Supporting Information

Length and thickness dependent optical response of liquid-exfoliated transition metal dichalcogenides

Kevin Synnatschke,[1] Patrick Arthur Cieslik,[1] Andrew Harvey,[2] Andres Castellanos-Gomez,[3] Tian Tian,[4] Chih-Jen Shih,[4] Alexey Chernikov,[6] Elton J. G. Santos,[5*] Jonathan N. Coleman,[2*] Claudia Backes[1*]

[1]*Institute for Physical Chemistry, Heidelberg University, D-69120 Heidelberg, Germany*

[2]*School of Physics and CRANN & AMBER Research Centres, Trinity College Dublin, Dublin 2, Ireland*

[3]*Materials Science Factory. Instituto de Ciencia de Materiales de Madrid (ICMM-CSIC), Madrid, E-28049, Spain*

[4]*Institute for Chemical and Bioengineering, ETH Zürich, 8093 Zürich, Switzerland*

[5]*School of Mathematics and Physics, Queen's University Belfast, BT7 1NN, United Kingdom*

[6]*Department of Physics, University of Regensburg, Regensburg D-93040, Germany.*

*E.Santos@qub.ac.uk

*colemaj@tcd.ie

*backes@uni-heidelberg.de

Content

1 Microscopy 3
1.1 AFM images, lateral dimensions (L, W) and number of layer distribution histograms 3
1.1.1 WS_2 4
1.1.2 MoS_2 4
1.1.3 WSe_2 5
1.1.4 $MoSe_2$ 6
1.2 Transmission electron microscopy 7
1.3 Tabulated values of nanosheet dimensions in each fraction 8
1.4 Correction of lateral dimensions from AFM 9
1.5 Relation of arithmetic and volume fraction-weighted mean layer number 10
2 Spectroscopy 11
2.1 Extinction and absorbance spectra of the LPE samples 11
2.1.1 Extinction coefficient spectra 12
2.1.2 Extinction and absorbance spectra of WS_2 13
2.1.3 Extinction and absorbance spectra of MoS_2 14
2.1.4 Extinction and absorbance spectra of WSe_2 15
2.1.5 Extinction and absorbance spectra of $MoSe_2$ 17
2.2 Photoluminescence spectra 19
2.3 Comparison of LPE samples to micromechanically-exfoliated nanosheets 20
2.3.1 Comparison of extinction/absorbance/reflectance spectra 20
2.3.2 Impact of scattering of LPE nanosheets on exciton energy vs. layer number 21
2.3.3 Exciton energy vs. layer number from different sample types and measurements 23
2.4 Solvent effects on A-exciton response 25
3 Supporting references 27

1 Microscopy

1.1 AFM images, lateral dimensions (L, W) and number of layer distribution histograms

In the following, representative AFM images of the size-selected fractions of the four transition metal dichalcogenides under study are shown along with their length (L) and layer number (N) distribution histograms. In each dispersion, 200-350 nanosheets were measured, and their length (longest dimension), width (dimension perpendicular to length) and thickness recorded. Some care must be taken when analysing the statistical nanosheet-height data. This is because the apparent AFM height of liquid-exfoliated nanosheets is typically larger than the theoretical thickness of the nanosheets due to adsorbed/intercalated water and surfactant. It is therefore important to know the apparent height of a single layer measured between terraces of incompletely exfoliated nanosheets (step height analysis). In previous reports, we found the step height of both MoS_2[1] and WS_2[2] to be 1.9 nm. Thus, to convert the measured AFM thickness to layer number, the height of the nanosheets was divided by 1.9 nm.

In all cases, the same cascade as detailed in the methods section was used for the size selection. For the selenides, the fraction of smallest/thinnest nanosheets (22-74k *g*) could not be analysed reliably by AFM statistics. For WS_2 and MoS_2, data from our previously published work[1, 2] was included in the plots in the main manuscript that show the scaling of nanosheet dimensions with optical properties.

In a standard size selection cascade, both length and thickness simultaneously decrease with increasing centrifugal force as characteristic power law (see figure 1, main manuscript). This results in a well-defined scaling of the <L>/<N> aspect ratios.[2, 3] As shown previously, this scaling of <L> and <N> can be overcome – to some extent – by changing the centrifugation conditions, for example in secondary cascades.[2] In a few reported cases,[3, 4] it was demonstrated that a much longer centrifugation (overnight) at a *g*-force lower than the initial boundary can be used to decouple the <L>-<N> relationship. Therefore, three fractions (0.1-0.4k *g*, 0.4-1k *g* and 1-5k *g*) of the selenide dispersions were subjected to an overnight centrifugation (14 h) at 25 *g*, 80 *g* and 200 *g*, respectively and the supernatant analysed.

1.1.1 WS_2

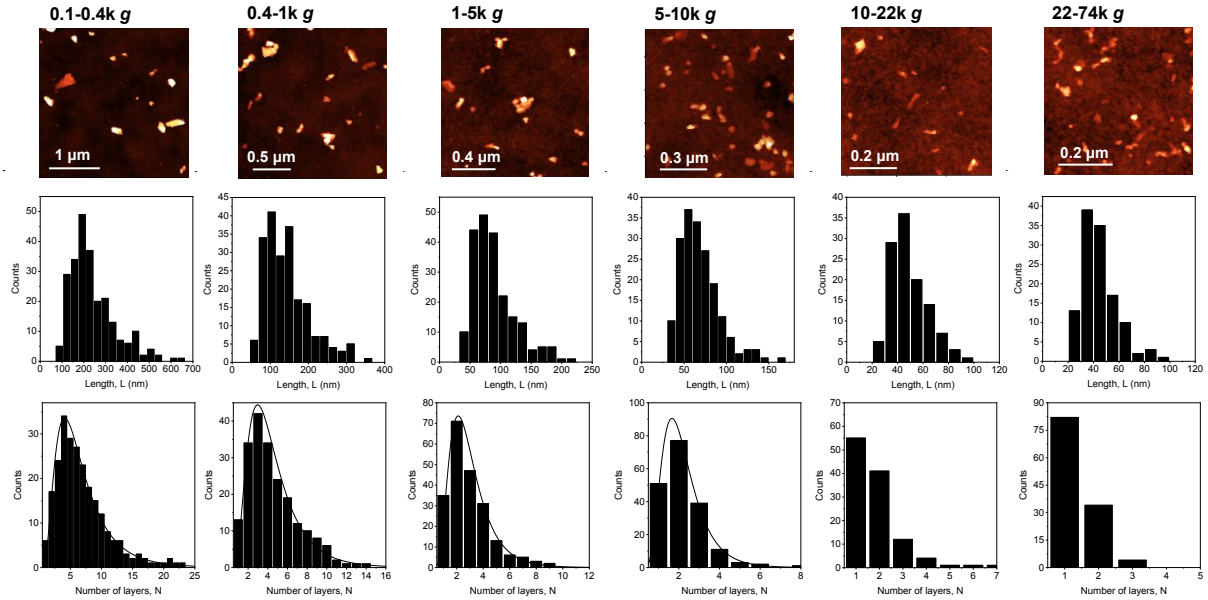

Figure S1: AFM analysis of the WS_2 fractions obtained with the standard cascade. Top row: representative images of the fractions isolated at the centrifugal acceleration indicated. Distribution histograms of i) second row: longest lateral dimension, length, *L*, (in nm), ii), third row: layer number *N*.

1.1.2 MoS_2

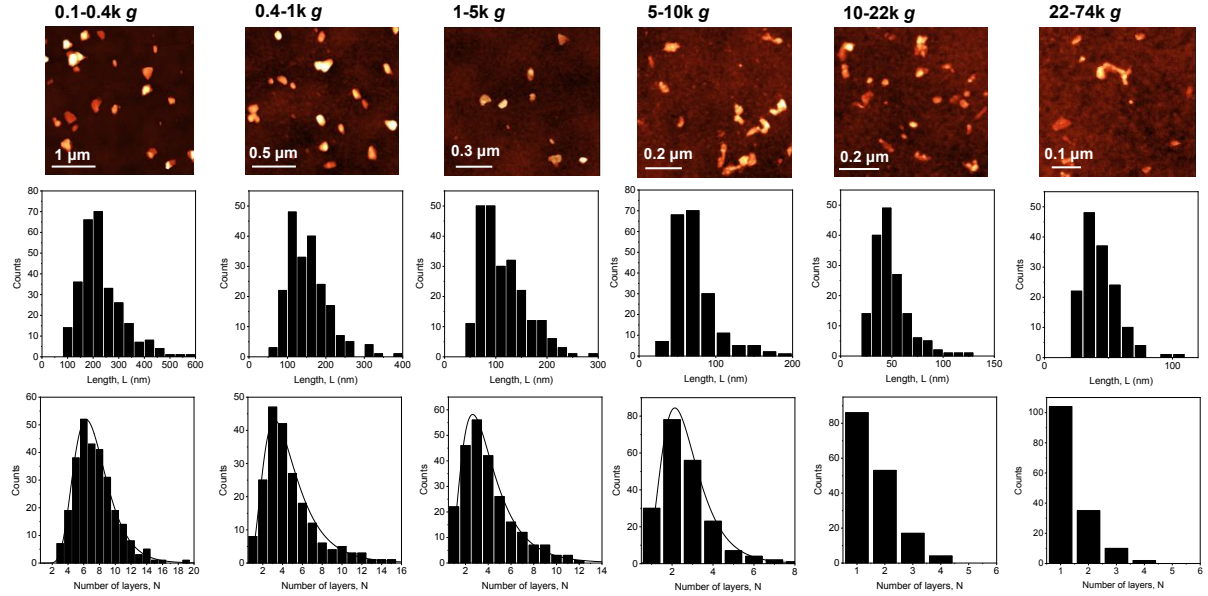

Figure S2: AFM analysis of the MoS_2 fractions obtained with the standard cascade. Top row: representative images of the fractions isolated at the centrifugal acceleration indicated. Distribution histograms of i) second row: longest lateral dimension, length, *L*, (in nm), ii), third row: layer number *N*.

1.1.3 WSe_2

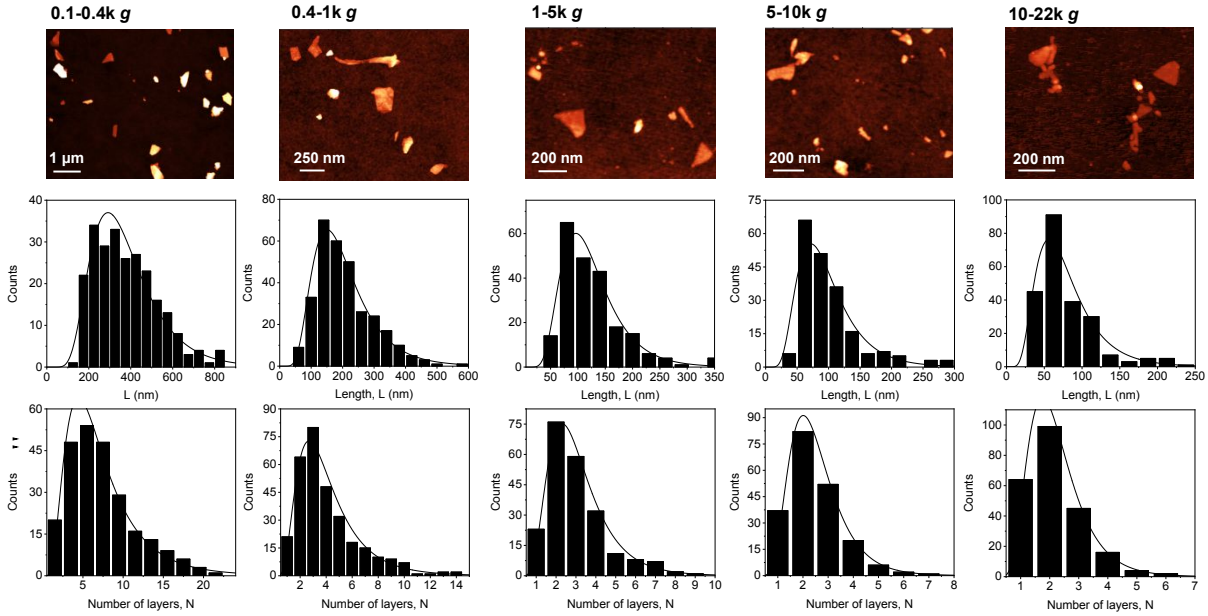

Figure S3: AFM analysis of the WSe_2 fractions obtained with the standard cascade. Top row: representative images of the fractions isolated at the centrifugal acceleration indicated. Distribution histograms of i) second row: longest lateral dimension, length, *L*, (in nm), ii), third row: layer number *N*.

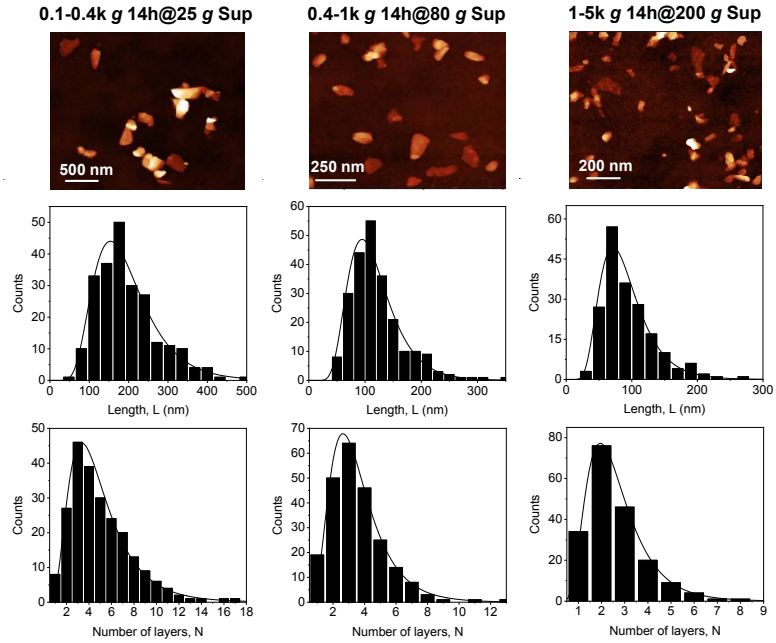

Figure S4: AFM analysis of the WSe_2 fractions obtained after overnight centrifugation. Top row: representative images of the fractions isolated at the centrifugal acceleration indicated. Distribution histograms of i) second row: longest lateral dimension, length, *L*, (in nm), ii), third row: layer number *N*.

1.1.4 $MoSe_2$

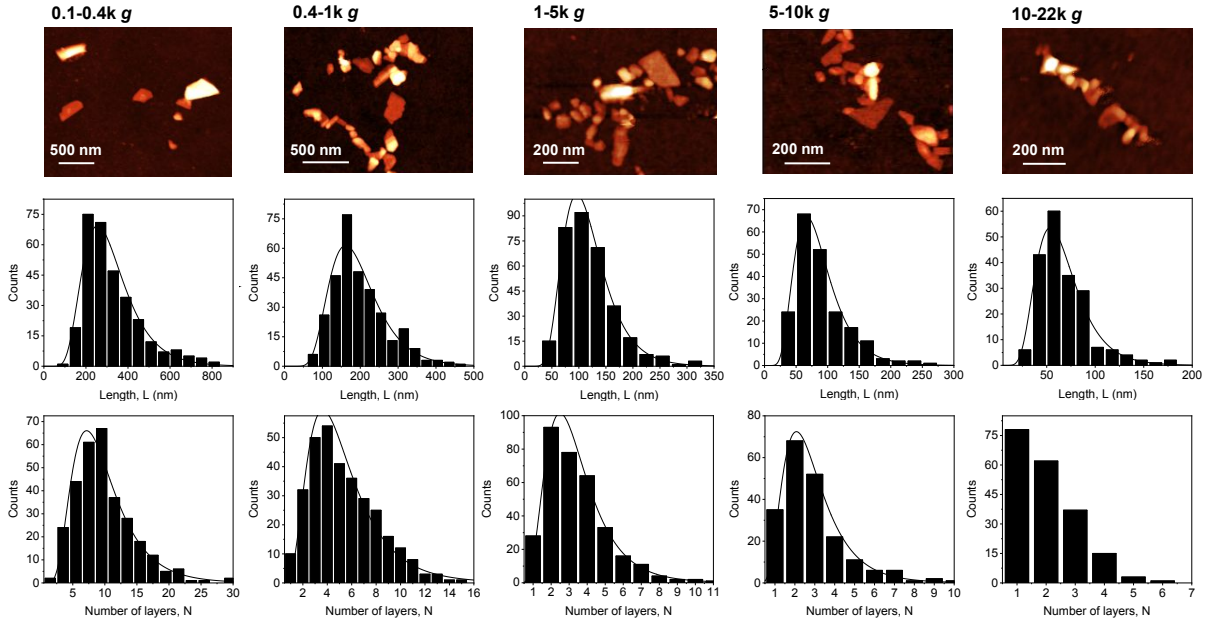

Figure S5: AFM analysis of the $MoSe_2$ fractions obtained with the standard cascade. Top row: representative images of the fractions isolated at the centrifugal acceleration indicated. Distribution histograms of i) second row: longest lateral dimension, length, *L*, (in nm), ii), third row: layer number *N*.

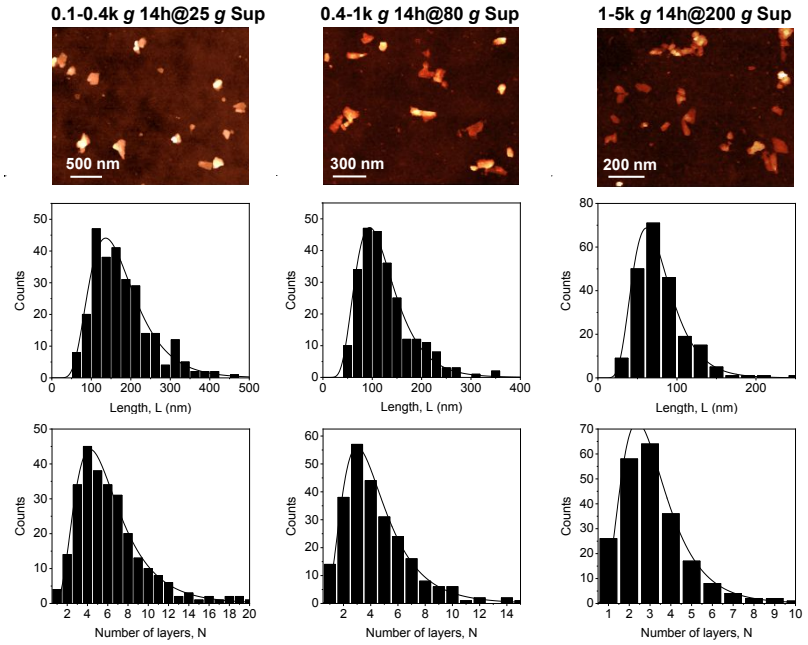

Figure S6: AFM analysis of the $MoSe_2$ fractions obtained after overnight centrifugation. Top row: representative images of the fractions isolated at the centrifugal acceleration indicated. Distribution histograms of i) second row: longest lateral dimension, length, *L*, (in nm), ii), third row: layer number *N*.

1.2 Transmission electron microscopy

Since size selection of WSe_2 and $MoSe_2$ using cascade centrifugation has not been previously demonstrated, the fractions were also characterised by transmission electron microscopy. Electron transparent nanosheets were observed in all cases that resemble the objects imaged in AFM. The length of 100-200 nanosheets was measured in each fraction. Representative images and the distribution histograms are shown below.

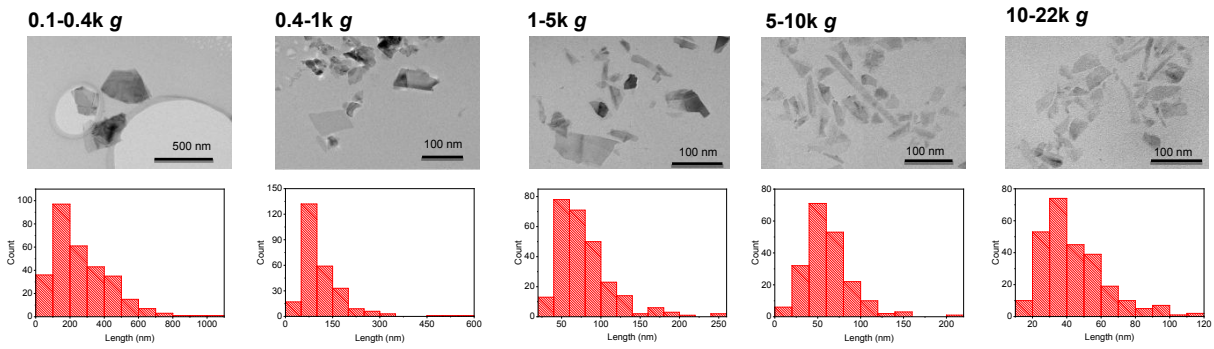

Figure S7: TEM analysis of the WSe_2 fractions obtained with the standard cascade. Top row: representative images of the fractions isolated at the centrifugal acceleration indicated. Bottom row: Distribution histograms of the longest lateral dimension, length, *L*.

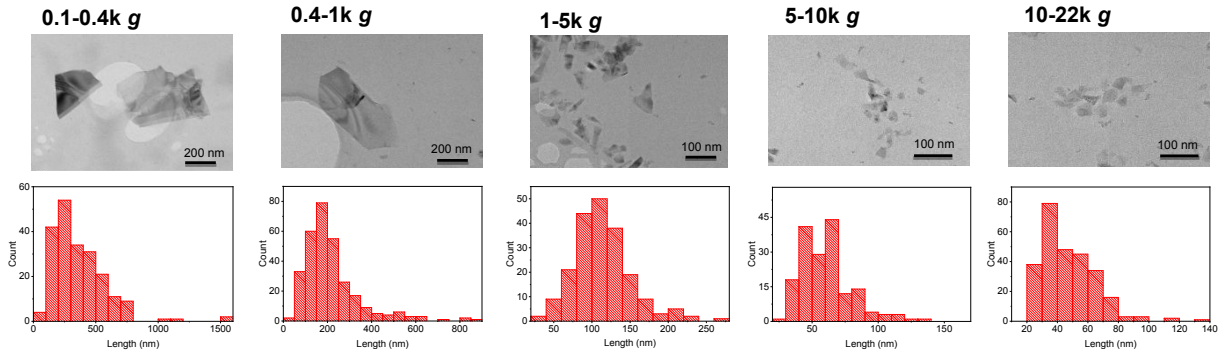

Figure S8: TEM analysis of the $MoSe_2$ fractions obtained with the standard cascade. Top row: representative images of the fractions isolated at the centrifugal acceleration indicated. Bottom row: Distribution histograms of the longest lateral dimension, length, *L*.

1.3 Tabulated values of nanosheet dimensions in each fraction

Table S1: Tabulated mean lateral size <L>, arithmetic mean layer number <N> and volume fraction weighted mean layer number $\langle N \rangle_{Vf}$ of the WS_2 samples as measured from AFM.

Sample	0.1-0.4k *g*	0.4-1k *g*	1-5k *g*	5-10k *g*	10-22k *g*	22-74k *g*
AFM <L>	240 nm	144 nm	90 nm	65 nm	46 nm	41 nm
AFM <N>	6.9	4.6	3.0	2.2	1.9	1.4
AFM $\langle N \rangle_{Vf}$	9.6	6.5	4.0	3.0	2.2	1.6

Table S2: Tabulated mean lateral size <L>, arithmetic mean layer number <N> and volume fraction weighted mean layer number $\langle N \rangle_{Vf}$ of the MoS_2 samples as measured from AFM.

Sample	0.1-0.4k *g*	0.4-1k *g*	1-5k *g*	5-10k *g*	10-22k *g*	22-74k *g*
AFM <L>	225 nm	150 nm	110 nm	68 nm	45 nm	40 nm
AFM <N>	7.7	4.8	3.8	2.7	1.8	1.5
AFM $\langle N \rangle_{Vf}$	11.2	7.8	5.7	3.2	2.2	1.6

Table S3: Tabulated mean lateral size <L>, arithmetic mean layer number <N> and volume fraction weighted mean layer number $\langle N \rangle_{Vf}$ of the WSe_2 samples as measured from AFM as well as <L> determined from TEM.

Sample	0.1-0.4k *g*	0.4-1k *g*	1-5k *g*	5-10k *g*	10-22k *g*	0.1-0.4k *g* 25*g* Sup	0.4-1k *g* 80*g* Sup	1-5k *g* 200*g* Sup
AFM <L>	380 nm	200 nm	125 nm	100 nm	80 nm	196 nm	117 nm	90 nm
TEM <L>	270 nm	120 nm	80 nm	63 nm	45 nm			
AFM <N>	7.3	4.2	3.2	2.6	2.2	5.0	3.6	2.7
AFM $\langle N \rangle_{Vf}$	10.3	6	3.8	2.6	2.3	6.6	4.6	3.2

Table S4: Tabulated mean lateral size <L>, arithmetic mean layer number <N> and volume fraction weighted mean layer number $\langle N \rangle_{Vf}$ of the $MoSe_2$ samples as measured from AFM as well as <L> determined from TEM.

Sample	0.1-0.4k *g*	0.4-1k *g*	1-5k *g*	5-10k *g*	10-22k *g*	0.1-0.4k *g* 25*g* Sup	0.4-1k *g* 80*g* Sup	1-5k *g* 200*g* Sup
AFM <L>	320 nm	200 nm	120 nm	87 nm	67 nm	176 nm	122 nm	77 nm
TEM <L>	310 nm	185 nm	110 nm	65 nm	47 nm			
AFM <N>	9.9	5.4	3.5	2.9	2.2	6.2	4.5	3.2
AFM $\langle N \rangle_{Vf}$	12.9	7.4	4.3	3.5	2.5	8.9	6.2	4.2

1.4 Correction of lateral dimensions from AFM

In general, the measurement of lateral sizes is over-estimated in AFM opposed to TEM (see table S3-S4). This is due tip broadening effects on the one hand and the result of the resolution which depends on the number of pixels of the image on the other hand. While tip broadening effects are expected to overestimate the lateral size by a constant factor, the broadening due to pixilation will depend on the image size and resolution used. To determine <L> from AFM which is required to extract $\langle N \rangle_{Vf}$ as accurately as possible, we have corrected the lateral dimensions measured by AFM through the remainder of the study with the empirical relation shown in figure S9 where we plot the mean length <L> measured by AFM *versus* <L> measured by TEM.

The data for MoS_2 and WS_2 in figure S9 is from previously published work.[1, 2] While we note that this correction is not a general relation, but related to instrument, scanning parameters and type of cantilever, it is remarkable that the data of this and previous work falls on a similar curve even though different AFM instruments and cantilevers were used. The combined data can be fit to a linear function with a slope of 1.05 and an intercept of 21 nm (which agrees well twice the value of the cantilever radius of 10 nm). We argue that the slope is due to the pixilation, while the intercept is a result of the tip broadening. The corrected AFM length is therefore related to the measured length by $L_{corrected} = L_{measured}/1.05 - 21$ nm.

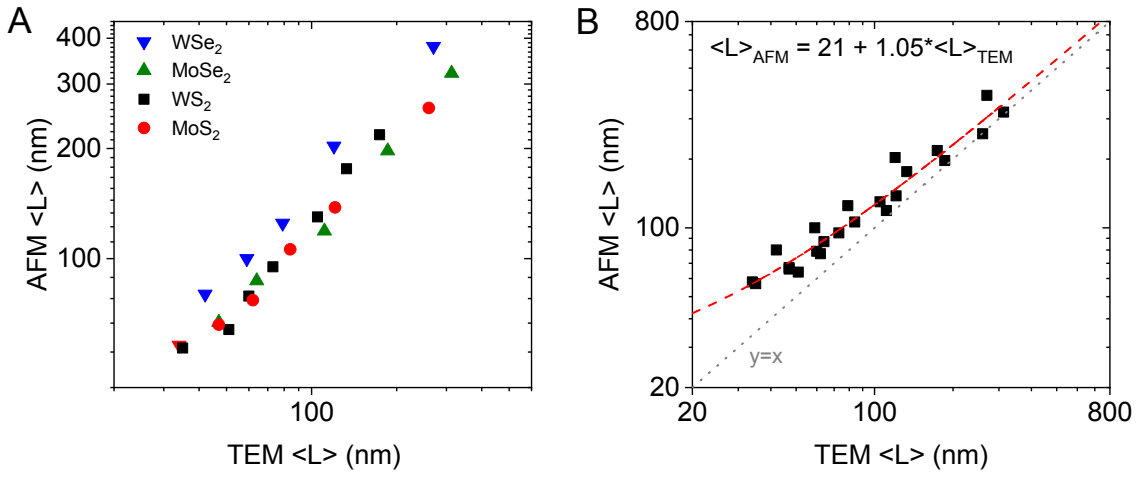

Figure S9: Correction of AFM lateral dimensions. A) Plot of statistically determined <L> from AFM versus <L> from TEM for fractions of the different transition metal dichalcogenides. MoS_2 and WS_2 data is from previously published work[1, 2] measured with a different AFM setup than the data of this work. B) Fit of all combined data giving a widely applicable correction of the lateral dimensions measured from AFM.

1.5 Relation of arithmetic and volume fraction-weighted mean layer number

Typically, the mean layer number of nanosheets in a dispersion is expressed as arithmetic mean layer number. However, spectroscopy probes the average volume/mass of the constituents in the dispersion. The goal of this study is to understand excitonic shifts with layer number on a more quantitative level than previous work. Therefore, we decided to express the layer number as volume fraction-weighted average ($\langle N \rangle_{Vf}$). Note that this is only possible when the overestimated lateral dimensions from AFM are corrected (see above). Even though $\langle N \rangle_{Vf}$ is larger than the arithmetic mean ($\langle N \rangle$), the arithmetic mean is still an equally adequate descriptor for the average nanosheet layer number because $\langle N \rangle$ and $\langle N \rangle_{Vf}$ are related as shown in figure S10.

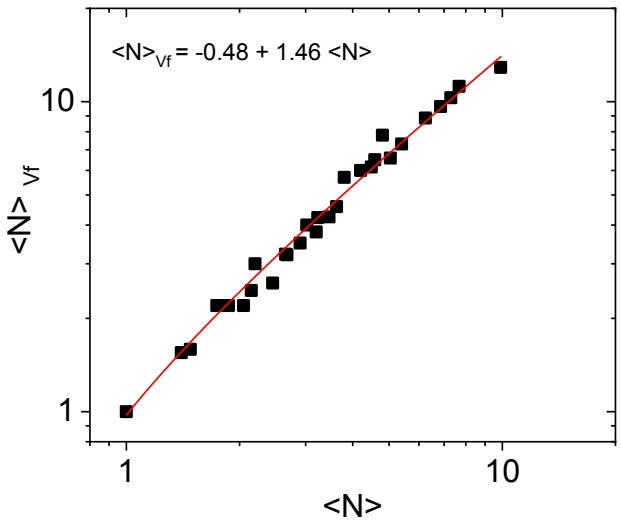

Figure S10: Relation of the volume fraction-weighted layer number to the arithmetic mean layer number.

2 Spectroscopy

2.1 Extinction and absorbance spectra of the LPE samples

Extinction coefficient spectra (figure S11) and normalised absorbance and extinction spectra (Figures S12-15) are shown for each material below. Since the A-exciton is superimposed on a background of varying intensity (from B exciton, as well as scattering in case of extinction spectra), it is not feasible to read off the peak positions from the spectra. One strategy is to fit the data as outlined in [5]. However, there can also be an error associated with fitting the spectra with multiple peaks.

We therefore take the approach of calculating the second derivative in the spectral region of the A-exciton. This gives a negative peak with contributions from the background widely eliminated. For calculating the second derivative, it is typically required to smooth the data (unless long integration times for the measurements are used which are more time consuming and thus not practical). However, smoothing has to be done with care. The impact of different smoothing methods is discussed in more detail elsewhere.[6] Here, we first smooth the spectrum with the Lowess method (20 points per window), calculate the second derivative and then smooth the second derivative again with Adjacent Averaging (40 points per window). With this strategy, any potential fine-structure in the spectra cannot be resolved, but peak positions can be accurately determined.

2.1.1 Extinction coefficient spectra

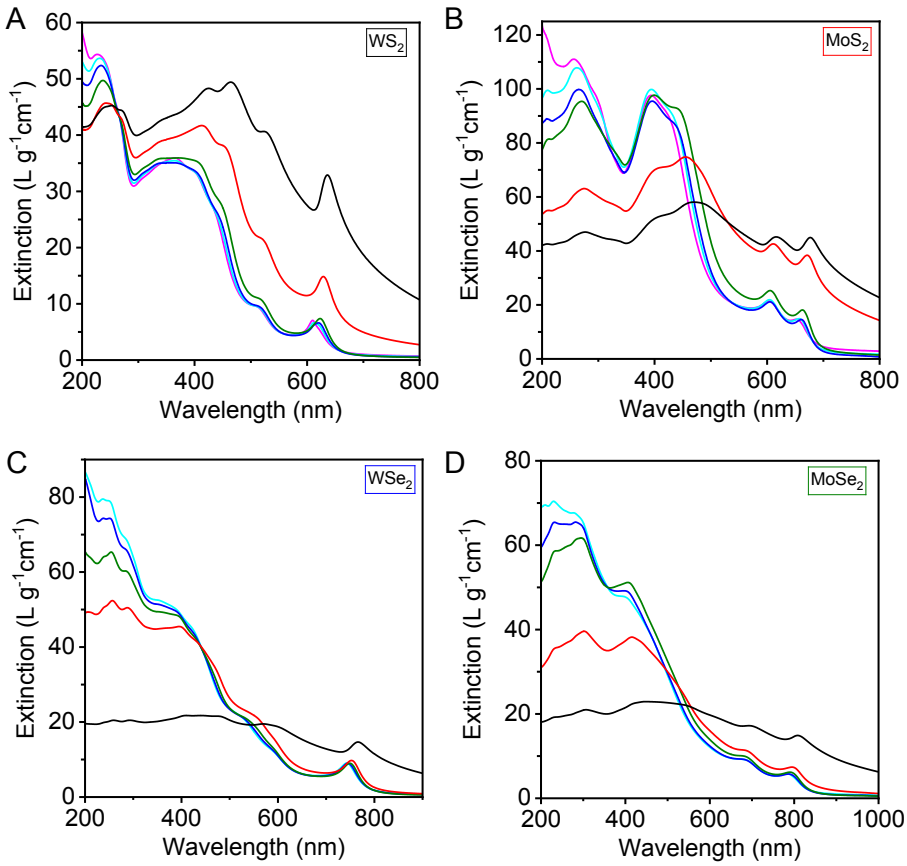

Figure S11: Extinction coefficient spectra of size-selected TMD dispersions. Decreasing size and thickness black-red-green-blue-cyan-magenta. A) WS_2, B) MoS_2, C) WSe_2, D) $MoSe_2$.

2.1.2 Extinction and absorbance spectra of WS_2

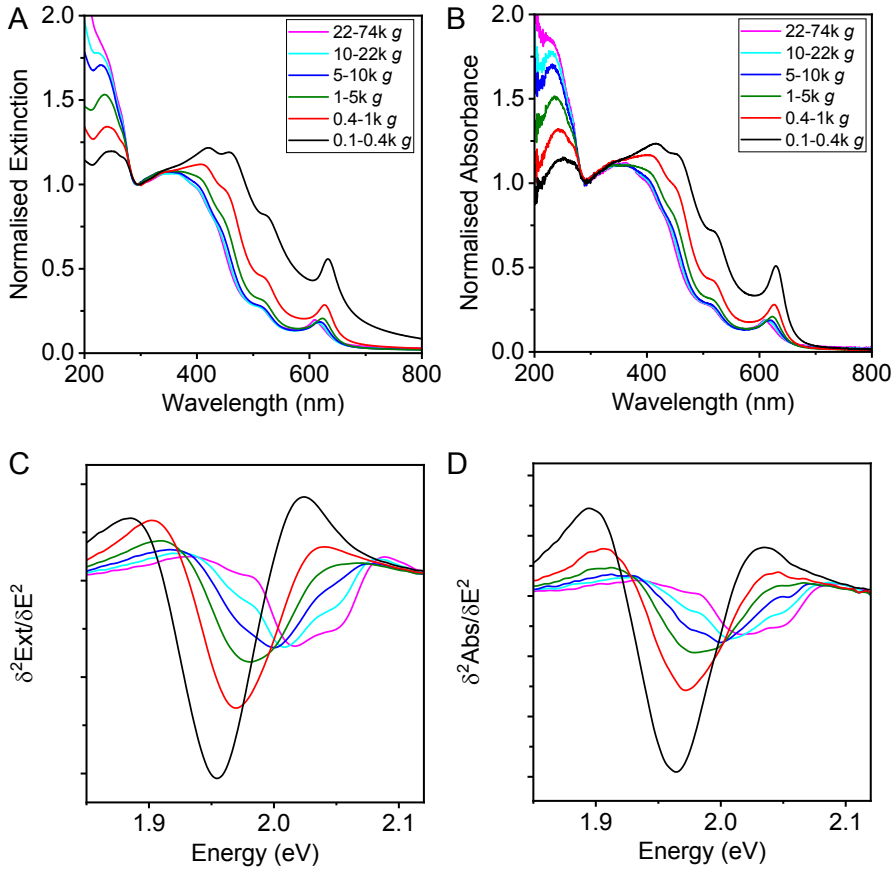

Figure S12: Normalised spectra of the WS_2 fractions. A) Extinction spectra, B) Absorbance spectra, C) Second derivative of the extinction spectrum in the A-exciton region, D) Second derivative of the absorbance spectrum in the A-exciton region.

2.1.3 Extinction and absorbance spectra of MoS_2

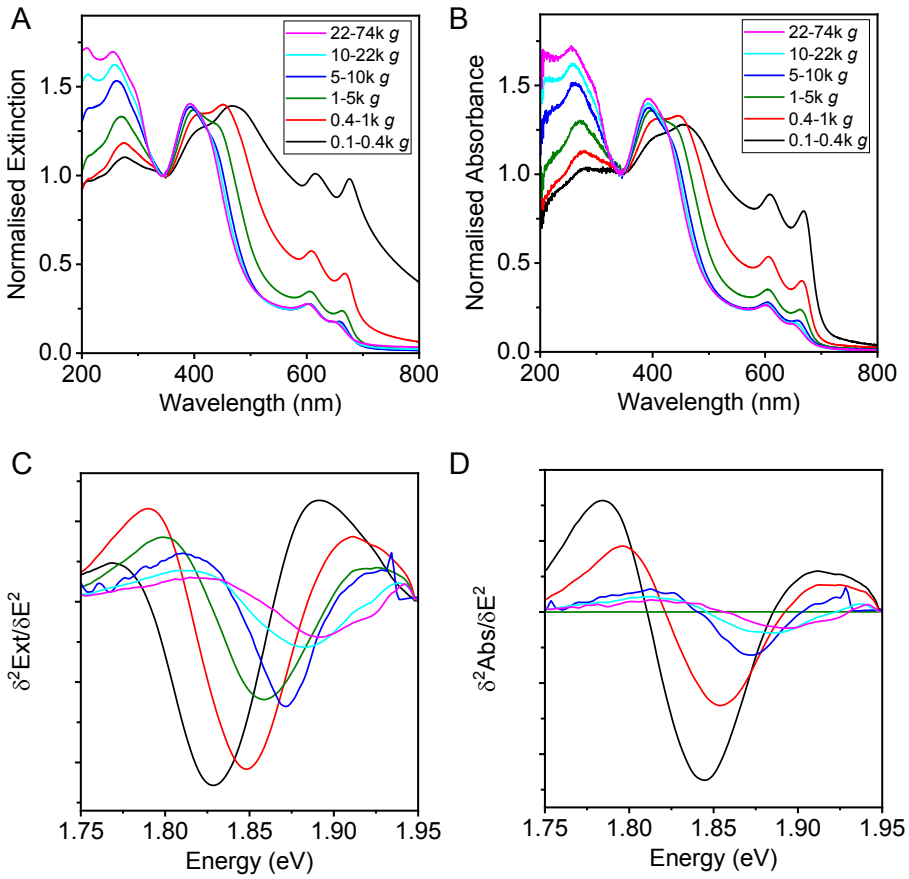

Figure S13: Normalised spectra of the MoS_2 fractions. A) Extinction spectra, B) Absorbance spectra, C) Second derivative of the extinction spectrum in the A-exciton region, D) Second derivative of the absorbance spectrum in the A-exciton region.

2.1.4 Extinction and absorbance spectra of WSe_2

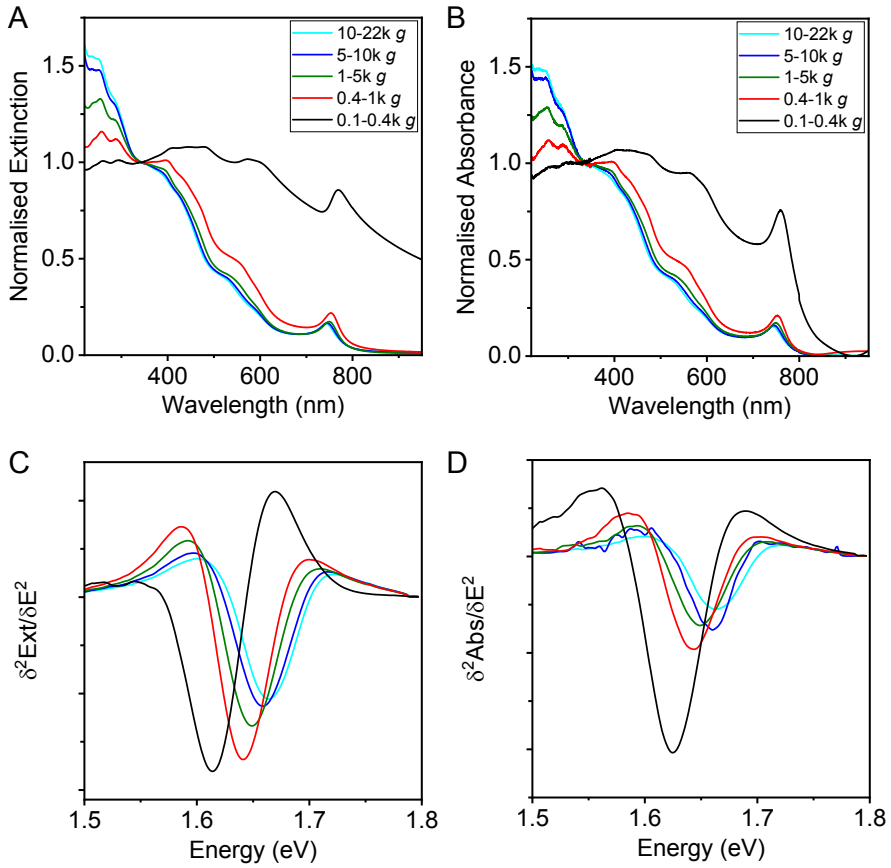

Figure S14: Normalised spectra of the WSe_2 fractions. A) Extinction spectra, B) Absorbance spectra, C) Second derivative of the extinction spectrum in the A-exciton region, D) Second derivative of the absorbance spectrum in the A-exciton region.

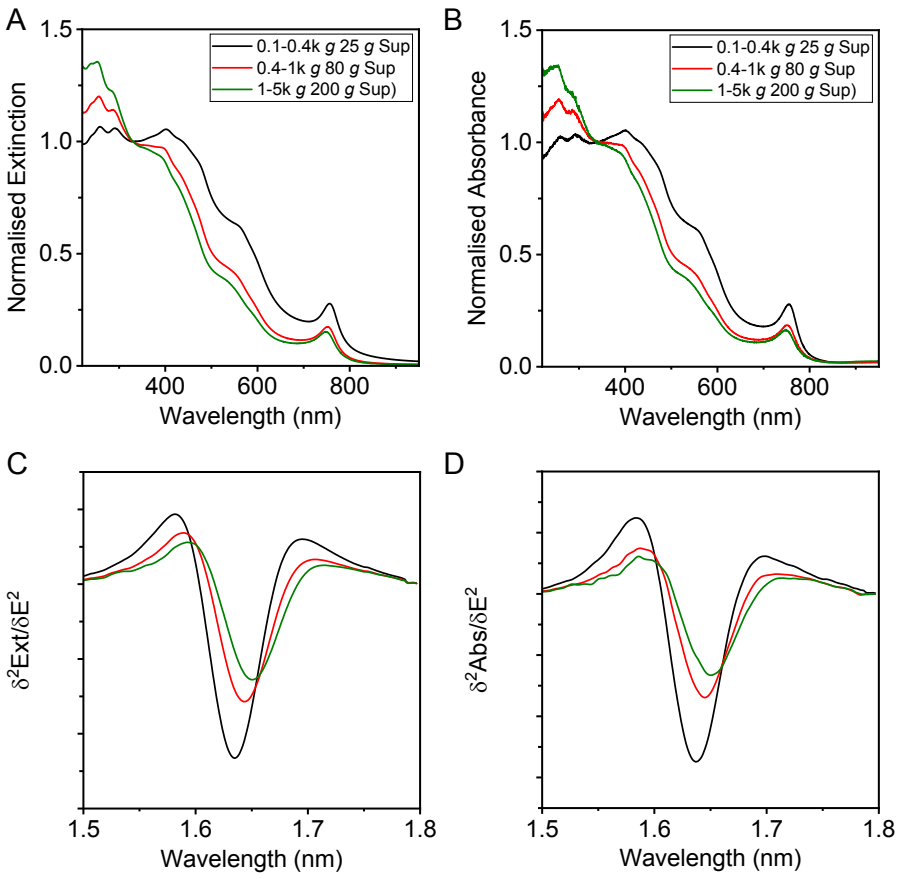

Figure S15: Normalised spectra of the WSe_2 fractions after overnight centrifugation. A) Extinction spectra, B) Absorbance spectra, C) Second derivative of the extinction spectrum in the A-exciton region, D) Second derivative of the absorbance spectrum in the A-exciton region.

2.1.5 Extinction and absorbance spectra of $MoSe_2$

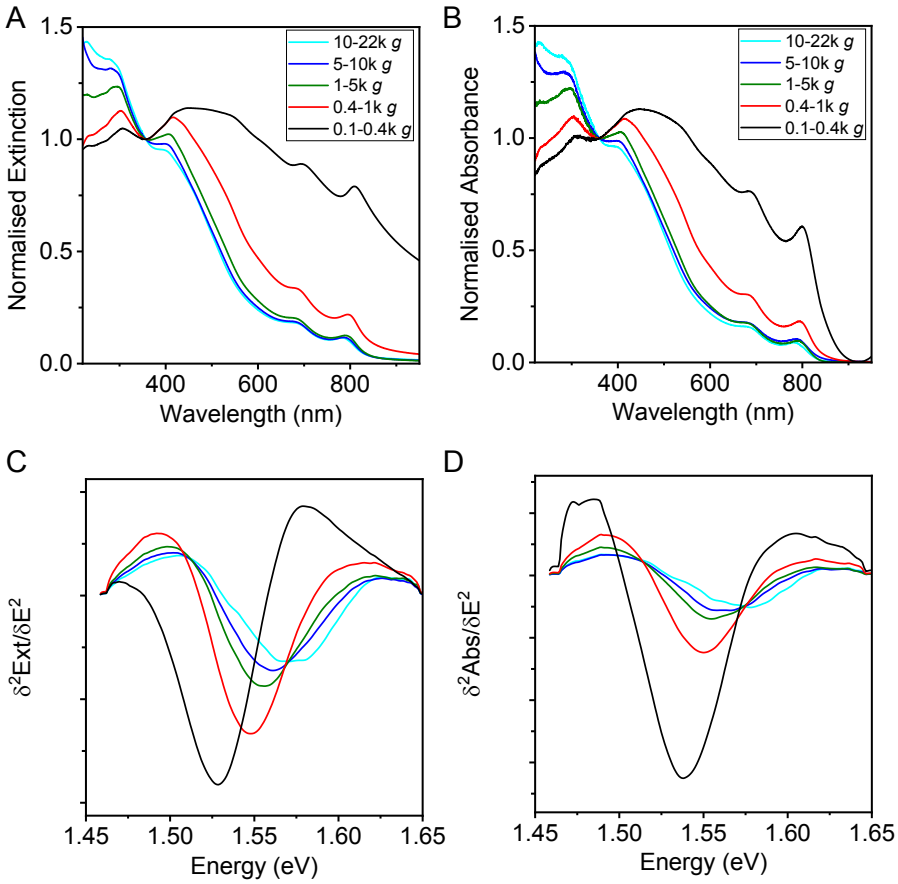

Figure S16: Normalised spectra of the $MoSe_2$ fractions. A) Extinction spectra, B) Absorbance spectra, C) Second derivative of the extinction spectrum in the A-exciton region, D) Second derivative of the absorbance spectrum in the A-exciton region.

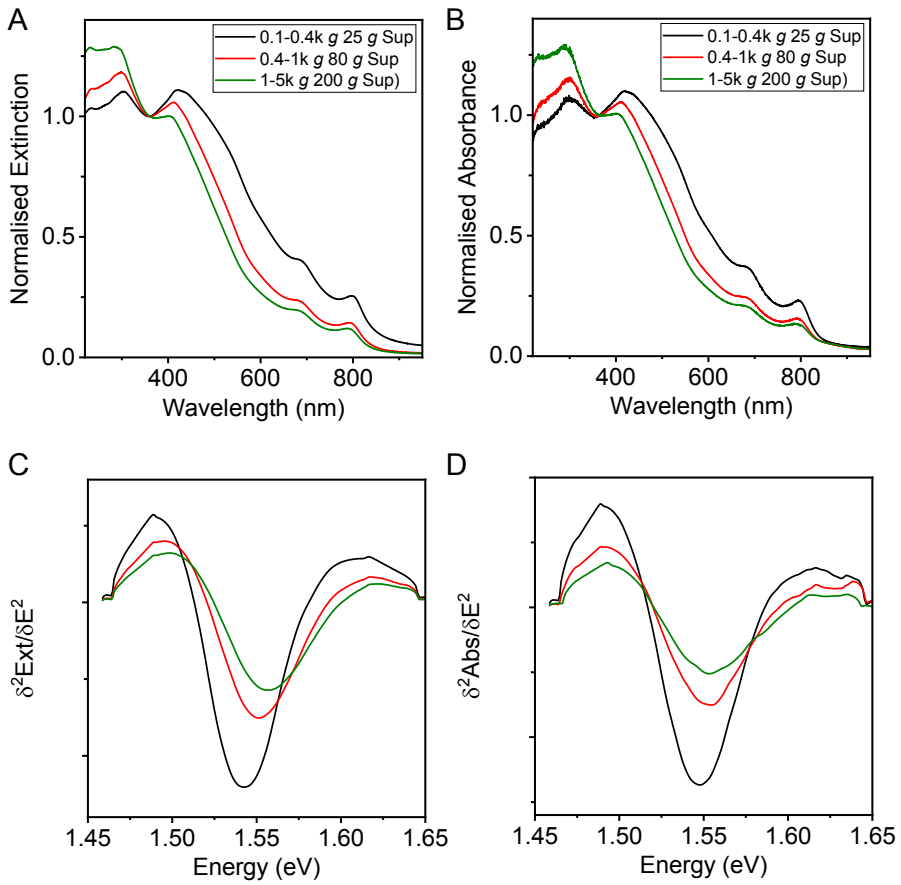

Figure S17: Normalised spectra of the $MoSe_2$ fractions after overnight centrifugation. A) Extinction spectra, B) Absorbance spectra, C) Second derivative of the extinction spectrum in the A-exciton region, D) Second derivative of the absorbance spectrum in the A-exciton region.

2.2 Photoluminescence spectra

Additional photoluminescence spectra (430 nm excitation) of the TMD dispersions are shown in figure S18. In each case, different fractions isolated at > 5000 *g* with equal concentrations are compared. In the fractions isolated at lower centrifugal acceleration, no A-exciton photoluminescence could be observed with this fluorescence spectrometer setup. This is because monolayer contents are low (see figures S1, S2, S3, S5 and tables S1-4). Except for variations in intensity, no changes in the PL spectra with respect to width, shape or position across the fractions are observed. Even though the monolayer contents in the 22-74k *g* fraction are highest, the PL intensity is typically lower than in the 10-22k *g* samples. We believe that this is because these nanosheets are also laterally smaller (~ 20 nm) and edge sites lead to nonradiative decay.

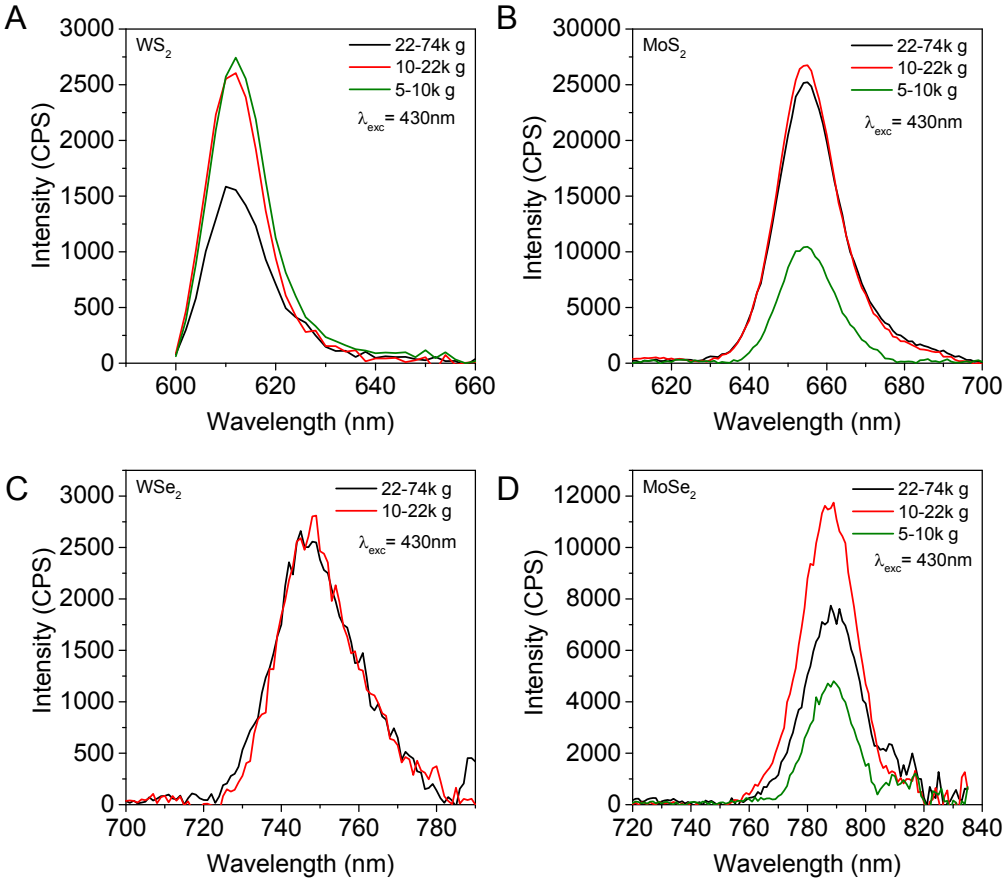

Figure 18 Photoluminescence spectra of different TMD fractions excited with 430 nm. A) WS_2, B) MoS_2, C) WSe_2, D) $MoSe_2$.

2.3 Comparison of LPE samples to micromechanically-exfoliated nanosheets

2.3.1 Comparison of extinction/absorbance/reflectance spectra

In the following, we compare extinction spectra acquired on nanosheet ensembles in dispersion after LPE and size selection with transmission/reflection spectra obtained on individual micromechanically-exfoliated nanosheets taken from literature.[5] Representative spectra for MoS_2 are shown in figure S19.

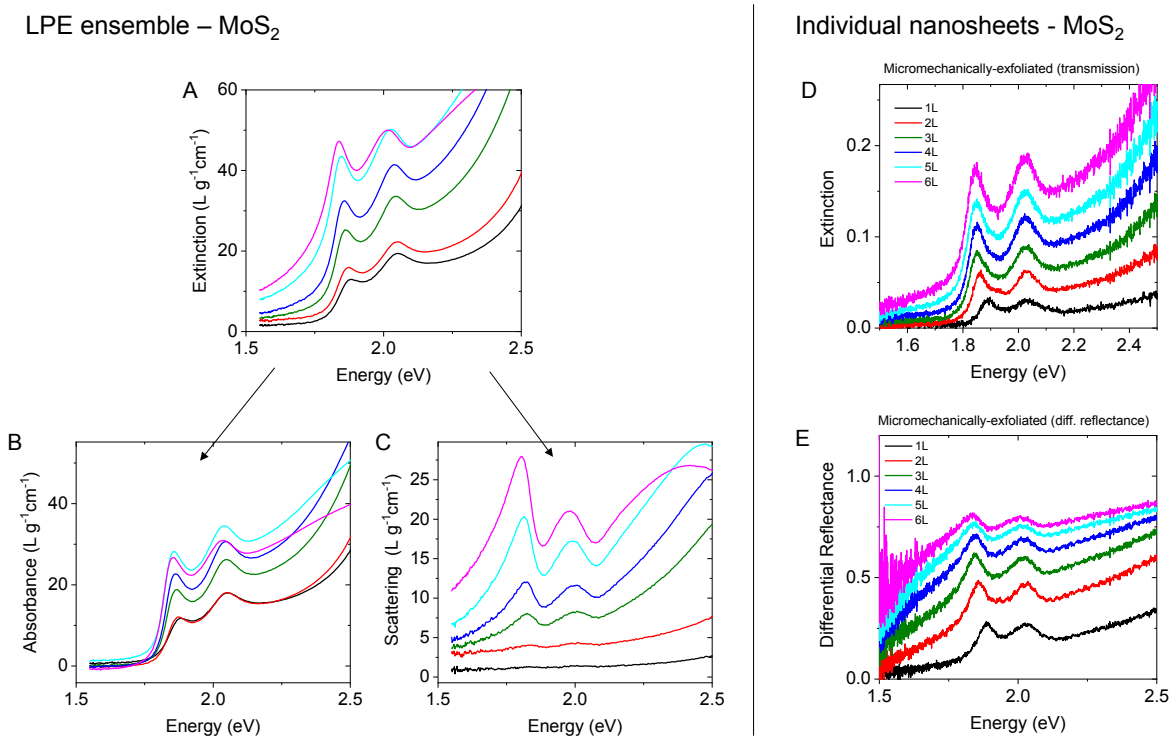

Figure S19: Comparison of extinction/absorbance/scattering spectra of LPE MoS_2 to transmission and differential reflectance spectra of micromechanically-exfoliated nanosheets. Left (A-C): Size selected liquid-exfoliated MoS_2 measured in dispersion. Right (D-E): individual micromechanically-exfoliated nanosheets measured on PDMS. A) Extinction spectra, B) absorbance spectra C) scattering spectra of LPE dispersions. D) Transmission (converted to extinction) spectra and E) differential reflectance spectra of individual MoS_2 nanosheets.

As also illustrated in the main manuscript, extinction spectra of fractions containing larger/thicker nanosheets can contain a significant contribution from light scattering. By a measurement in the centre of an integrating sphere, the scattered light is collected and absorbance spectra are obtained. As a result, the extinction spectra (e.g. figure S19A) can be deconvoluted into contributions from absorbance (figure S19B) and scattering (figure S19C). Both absorbance and scattering have a distinct shape. For example, the absorbance drops to 0 at energies below the A-exciton. Signal in the extinction spectra in this energy range is thus due

to scattering. Furthermore, scattering spectra in the resonant regime follow the absorbance in shape, but redshifted and with different relative intensities.

The transmission spectra (converted to extinction in figure S19D) of micromechanically-exfoliated nanosheets strongly resemble the extinction spectra of the dispersions in shape. For nanosheets > 3 layers, the extinction intensity does not drop to 0 at energies < 1.7 eV in contrast to the absorbance spectra of LPE nanosheets. In addition to direct reflectance, this could suggest that light scattering may also contribute to the signal in transmission spectra of micromechanically-exfoliated nanosheets. This contribution is stronger in the differential reflectance spectra (figure S19E), where a pronounced background is discernible already for the bilayer. In reflectance spectra, both the real and imaginary part of the dielectric function contribute depending on the substrate and optical sample thickness, while only the imaginary part is related to the absorbance. Therefore, it cannot be excluded that this background is due to a contribution from the real part of the dielectric function. However, we note that other published reflectance spectra[7-9] show less of a background suggesting that it is indeed partly due to scattering and therefore dependent on the setup used for the measurement.

2.3.2 Impact of scattering of LPE nanosheets on exciton energy vs. layer number

Since the scattering spectrum in the resonant regime is redshifted compared to the absorbance, it is expected that a contribution from scattering to extinction spectra has an impact on the exciton resonance energy. To test this, we plot the exciton energy from extinction and absorbance spectra as function of the volume fraction weighted mean layer number in figure S21. For WS_2 (figure S20A), the difference between data from extinction and absorbance is minor in agreement with previous findings.[2] For the other TMDs (figure S20B-D), the A-exciton energy measured in extinction clearly deviates from the absorbance data for dispersions with $\langle N \rangle_{Vf}$ greater than ~8-9 (which roughly related to $\langle L \rangle$ > 200 nm). In particular, the A-exciton energy keeps decreasing with increasing layer number beyond 10 layers where the bulk value has already been reached for the absorbance data. Practically this means that care must be taken to apply the spectroscopic metrics to extinction spectra for samples > 10 layers because peak shifts are no longer related to confinement and dielectric screening effects, but to an increasing contribution from light scattering which is also dependent on the lateral dimensions of the nanosheets[3] and their thickness.

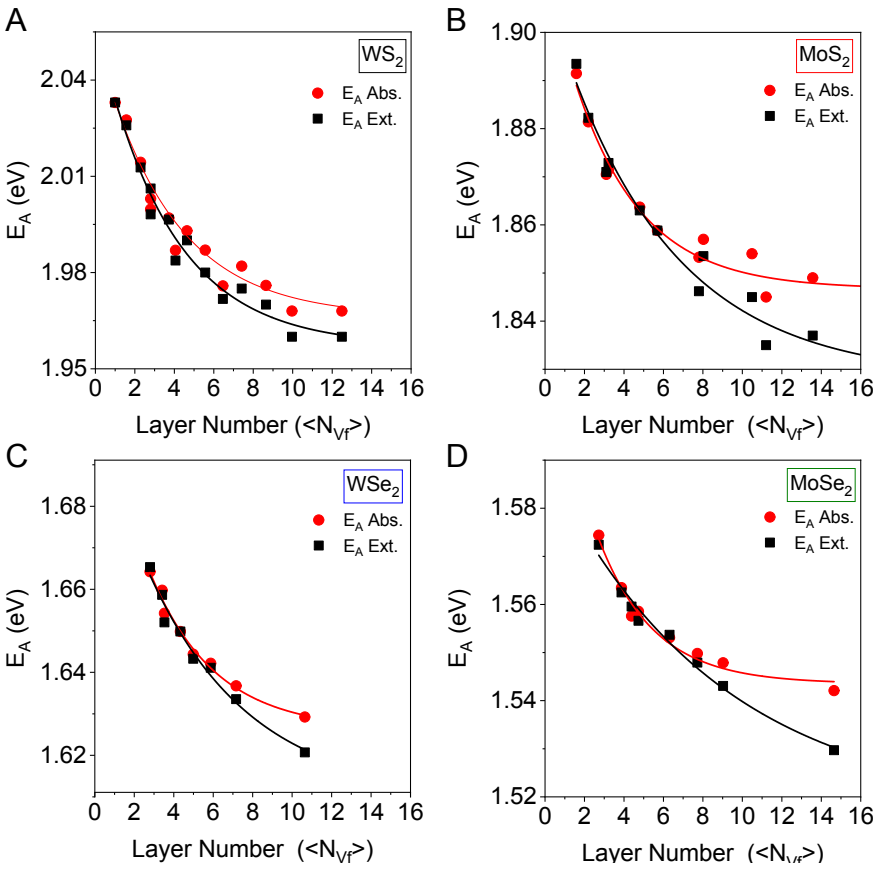

Figure S20: A-Exciton energies as function of nanosheet layer number from absorbance and extinction. A) LPE WS_2, B) LPE MoS_2, C) LPE WSe_2, D) LPE $MoSe_2$.

2.3.3 Exciton energy vs. layer number from different sample types and measurements

When comparing A-exciton energies from micromechanically-exfoliated nanosheets measured in differential reflectance to the data extracted from the absorbance spectra of the LPE dispersions, it is obvious that the A-exciton is at consistently lower energies in the differential reflectance data (figure S21). In addition, the bulk values are reached at 5-6 layers rather than ~ 10 layers as in the case of the LPE samples, i.e. N_0 is significantly lower. This could potentially be a manifestation of intercalated water/surfactant between the LPE nanosheets which changes the dielectric screening which we believe defines N_0 (see main manuscript). Interestingly, other reflectance data extracted from literature (magenta data points, see main manuscript) is very close to the LPE absorbance data, albeit with a significant scatter and some deviations in absolute energies.

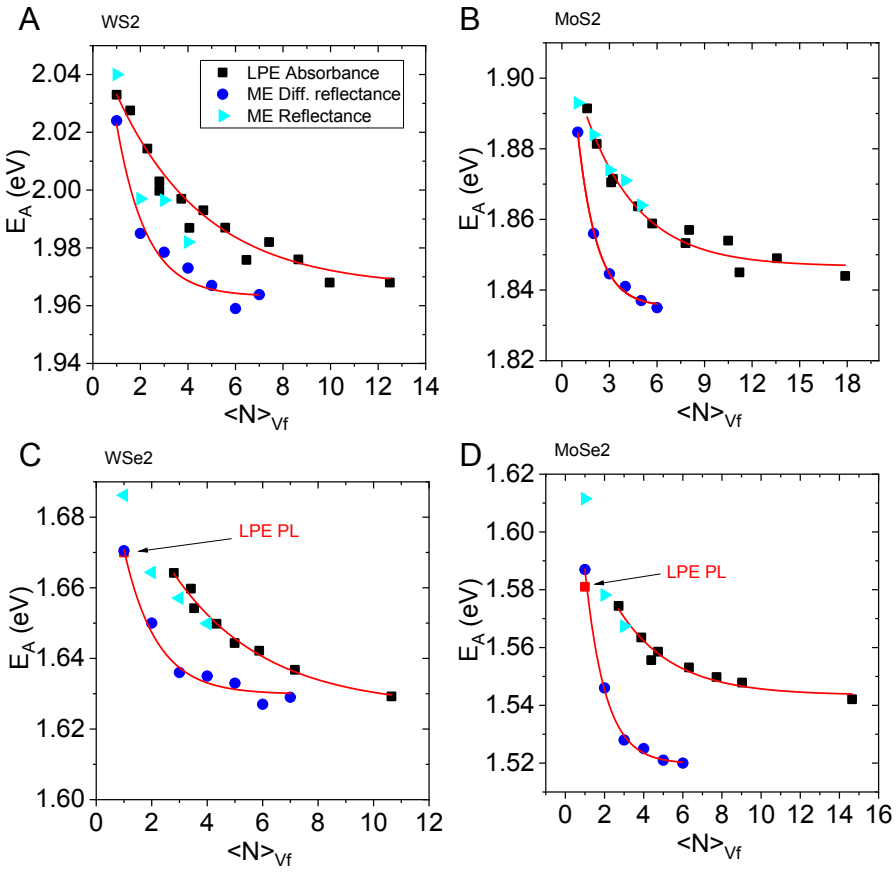

Figure S21: A-Exciton energies as function of nanosheet layer number from absorbance (LPE), reflectance as well as differential reflectance on micromechanically-exfoliated (ME) nanosheets. A) WS_2, B) MoS_2, C) WSe_2, D) $MoSe_2$. All spectra were analysed in the same way (smooth and derive) to extract the exciton energy. For the LPE selenides, the A-exciton energy of the (monolayer) photoluminescence is included (red data point), as they show a larger Stokes shift than the sulphides.

The difference between the data from differential reflectance and LPE absorbance likely has multiple origins. On the one hand, the sample types and measurements are completely different. For example, the micomechanically-exfoliated nanosheets are surrounded by PDMS on the one side and air on the other, while the LPE samples are in water surfactant. In addition, LPE nanosheets are quite small and can relax, while micromechanically-exfoliated nanosheets are larger and can be strained on the substrate. In addition, the temperature of the measurement in dispersion can be readily maintained at 20°C owing to the liquid environment and low power light, while heating can occur in the case of the micromechanically exfoliated nanosheets.

On the other hand, we believe that part of the discrepancy stems from contributions from scattering to the differential reflectance spectra. This is illustrated more clearly in the exciton energy extracted from various different measurements as function of layer number in figure S22 for MoS_2. The data from the transmission spectra of micromechanically-exfoliated nanosheets saturates at the same bulk values as the data extracted from the extinction spectra of the LPE samples (slightly lower value than the absorbance). This agrees well with the closely resembling spectra (see figure S19). In the case of the differential reflectance spectra, the A-exciton energy saturates at lower bulk exciton energy. In fact, the data is somewhere between the LPE absorbance and scattering. Since the sample type (see above) should not have an impact in extrapolated bulk exciton energies, this behaviour is likely related to scattering in the differential reflectance spectra.

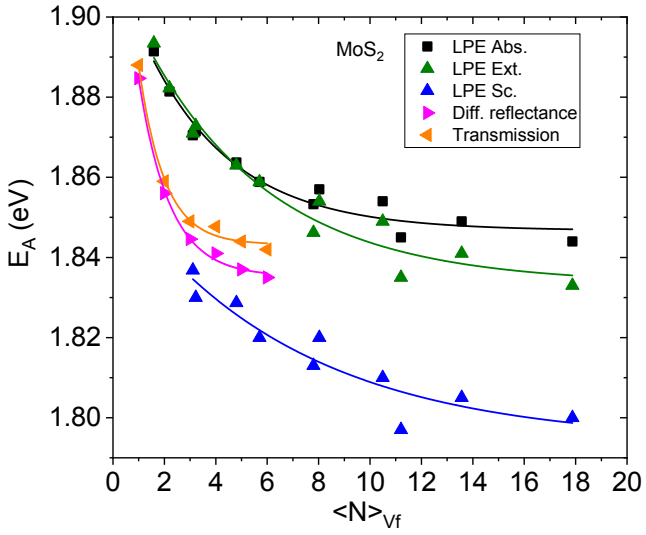

Figure S22: A-Exciton energies of MoS_2 as function of nanosheet layer number from various measurements including absorbance/extinction/scattering on LPE samples, differential reflectance and transmission on micromechanically-exfoliated nanosheets.

2.4 Solvent effects on A-exciton response

The A-exciton energies of liquid phase exfoliated nanosheets can be affected by the surrounding medium, i.e. the solvent. To test the magnitude of this effect, WS_2 was exfoliated and size-selected in aqueous sodium cholate (as before) and then transferred to different solvent system. This was achieved by centrifuging the size-selected fractions at centrifugal accelerations above the upper centrifugation boundary used for the size selection and redispersing the sediment in the respective solvent. The mean layer number of the sheets was calculated from the spectroscopic metrics of a reference sample redispersed in aqueous sodium cholate. Note that the choice of solvents is relatively limited, as not all solvents will give colloidally stable dispersions. Within the experimentally constraints, they were chosen to maximize differences in the dielectric constant (see table S5).

Figure S23 shows the A-exciton energy as function of layer number in the solvent systems compared to the aqueous sodium cholate reference. The A-exciton energies are red-shifted compared to the reference sample, but show similar rates of increasing A-exciton energies with decreasing layer number. The fit parameters to equation 4 in the main manuscript are summarized in table S5.

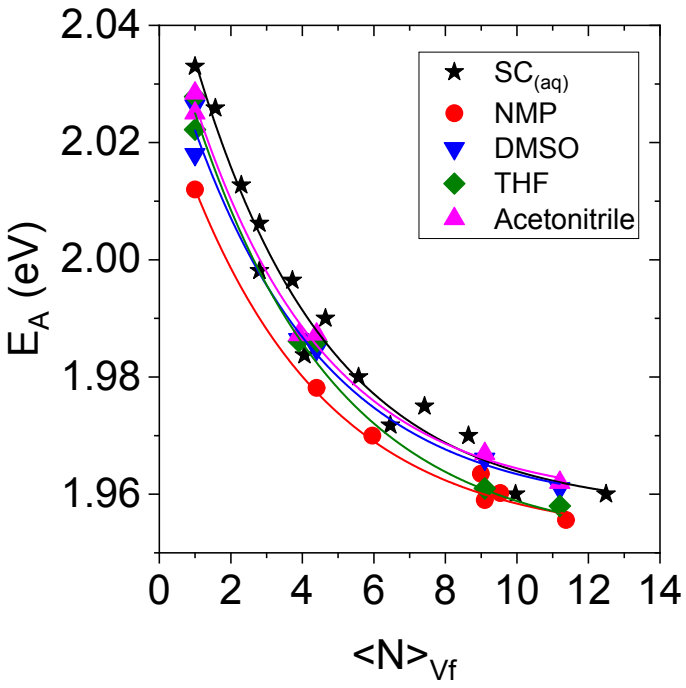

Figure S23: A-Exciton energies of WS_2 as function of nanosheet layer number from extinction after transfer into different solvents. The aqueous sodium cholate (black stars) is shown as reference for comparison with common organic solvents.

Table S5: Exponential decay fit parameters for A-exciton position versus mean nanosheet thickness (layer number) data in different solvents (from figure S23). The solvent dielectric constant is also given.

	Solvent dielectric constant	$E_{A,ML}$ (eV)	$E_{A,Bulk}$ (eV)	N_0
WS_2-SC	78.4 (water, 298 K)	2.033	1.966	3.72 ± 0.55
WS_2-NMP	33 (298 K)	2.012	1.952	3.91 ± 0.55
WS_2-DMSO	46.7 (298 K)	2.018	1.957	3.81 ± 0.80
WS_2-THF	7.6 (298 K)	2.025	1.951	3.94 ± 0.66
WS_2-Acetonitrile	37.5 (298 K)	2.027	1.959	3.65 ± 0.44

3 Supporting references

1. Backes, C.; Smith, R. J.; McEvoy, N.; Berner, N. C.; McCloskey, D.; Nerl, H. C.; O'Neill, A.; King, P. J.; Higgins, T.; Hanlon, D.; Scheuschner, N.; Maultzsch, J.; Houben, L.; Duesberg, G. S.; Donegan, J. F.; Nicolosi, V.; Coleman, J. N., Edge and Confinement Effects Allow in situ Measurement of Size and Thickness of Liquid-Exfoliated Nanosheets. *Nature Commun.* **2014,** 5, 4576.
2. Backes, C.; Szydłowska, B. M.; Harvey, A.; Yuan, S.; Vega-Mayoral, V.; Davies, B. R.; Zhao, P.-l.; Hanlon, D.; Santos, E. J. G.; Katsnelson, M. I.; Blau, W. J.; Gadermaier, C.; Coleman, J. N., Production of Highly Monolayer Enriched Dispersions of Liquid-Exfoliated Nanosheets by Liquid Cascade Centrifugation. *ACS Nano* **2016,** 10 1589-1601.
3. Harvey, A.; Backes, C.; Boland, J. B.; He, X.; Griffin, A.; Szydlowska, B.; Gabbett, C.; Donegan, J. F.; Coleman, J. N., Non-resonant light scattering in dispersions of 2D nanosheets. *Nature Commun.* **2018,** 9, 4553.
4. Griffin, A.; Harvey, A.; Cunningham, B.; Scullion, D.; Tian, T.; Shih, C.-J.; Gruening, M.; Donegan, J. F.; Santos, E. J. G.; Backes, C.; Coleman, J. N., Spectroscopic Size and Thickness Metrics for Liquid-Exfoliated h-BN. *Chem. Mater.* **2018,** 30, 1998-2005.
5. Niu, Y.; Gonzalez-Abad, S.; Frisenda, R.; Marauhn, P.; Drüppel, M.; Gant, P.; Schmidt, R.; Taghavi, N.; Barcons, D.; Molina-Mendoza, A.; de Vasconcellos, S.; Bratschitsch, R.; Perez De Lara, D.; Rohlfing, M.; Castellanos-Gomez, A., Thickness-Dependent Differential Reflectance Spectra of Monolayer and Few-Layer MoS2, MoSe2, WS2 and WSe2. *Nanomater.* **2018,** 8, 725.
6. Ueberricke, L.; Coleman, J. N.; Backes, C., Robustness of Size Selection and Spectroscopic Size, Thickness and Monolayer Metrics of Liquid-Exfoliated WS2. P*hys. Status Solidi (b)* **2017,** 254, 1700443.
7. Li, Y.; Chernikov, A.; Zhang, X.; Rigosi, A.; Hill, H. M.; van der Zande, A. M.; Chenet, D. A.; Shih, E.-M.; Hone, J.; Heinz, T. F., Measurement of the optical dielectric function of monolayer transition-metal dichalcogenides: MoS2, MoSe2, WS2, WSe2. *Phys. Rev. B* **2014,** 90, 205422.
8. Hill, H. M.; Rigosi, A. F.; Roquelet, C.; Chernikov, A.; Berkelbach, T. C.; Reichman, D. R.; Hybertsen, M. S.; Brus, L. E.; Heinz, T. F., Observation of Excitonic Rydberg States in Monolayer MoS2 and WS2 by Photoluminescence Excitation Spectroscopy. *Nano Lett.* **2015,** 15, 2992-2997.
9. Zhao, W.; Ghorannevis, Z.; Chu, L.; Toh, M.; Kloc, C.; Tan, P.-H.; Eda, G., Evolution of Electronic Structure in Atomically Thin Sheets of WS2 and WSe2. *ACS Nano* **2012,** 7, 791-797.